Journal of Power Sources 183 (2008) 771–782

Contents lists available at ScienceDirect

Journal of Power Sources

journal homepage: www.elsevier.com/locate/jpowsour

II. A combined model for determining capacity usage and battery size for hybrid and plug-in hybrid electric vehicles

Paul Albertus [a,*], Jeremy Couts [a], Venkat Srinivasan [b], John Newman [a]

[a] Department of Chemical Engineering, University of California, Berkeley, CA 94720-1462, USA
[b] Energy and Environmental Technologies Division, Lawrence Berkeley National Laboratory, USA

ARTICLE INFO

Article history:
Received 18 March 2008
Received in revised form 1 May 2008
Accepted 2 May 2008
Available online 9 May 2008

Keywords:
Hybrid electric vehicle
Plug-in hybrid electric vehicle
Lithium-ion battery
Modeling
Battery size
Capacity usage

ABSTRACT

We combine a detailed battery model with a simple vehicle model to examine the battery size and capacity usage of a $Li_xC_6/Li_{y+0.16}Mn_{1.84}O_4$ cell (with a normal and artificially flat equilibrium potential) and a $Li_{4+3x}Ti_5O_{12}/Li_yFePO_4$ cell. The features of cell chemistry we are concerned with are the magnitude and shape of the cell equilibrium potential and internal resistance. Our key findings include that a battery for a hybrid electric vehicle application has a capacity usage from 15 to 25% (for a minimum separator area size), and as one moves from a HEV battery to a plug-in hybrid electric vehicle battery there is a change in the slope of the separator area *vs.* equivalent-electric range curve due to the shape of the pulse-power capability. We also find that defining the resistance using the HPPC protocol has limitations because in general the pulse resistance depends on the applied current and pulse duration. Our detailed, combined model also shows that the benefits of a flat-potential system may be limited because of the relative positions of a flat and sloped equilibrium potential, and the lack of a driving force for the relaxation of solid-phase concentration gradients throughout the electrode. That latter effect is shown to be more significant for electrodes with a non-uniform current distribution.

1. Introduction

Because of their high energy and power density, lithium-ion batteries are the chemistry of choice for hybrid electric vehicle (HEV) and plug-in hybrid electric vehicle (PHEV) applications; their use has been limited thus far due to concerns about safety, life, and cost rather than performance. There is a wide variety of materials that can be used in lithium-ion batteries, and the details of the particular chemistry have an influence on the size of the battery that is required. Some of the important chemistry-specific factors include the shape and magnitude of the equilibrium potentials, the internal resistance (and its dependence on state-of-charge), and the specific capacities and densities. There are also geometric factors that influence battery size, including the thickness and porosity of the electrodes. In practice, there are tradeoffs among the different performance characteristics. For example, a lower resistance can be achieved by using an anode with a potential sufficiently high that no solid–electrolyte interphase (SEI) forms (*e.g.*, a $Li_{4+3x}Ti_5O_{12}$ negative electrode). In this study we combine a detailed battery model (Dualfoil) with a simple vehicle model to examine how the various features of cell chemistry affect battery size and capacity usage. The present work should be considered along with a simple model presented in a companion work [1].

The performance requirements for HEVs and PHEVs typically involve both power and energy requirements, which come from a vehicle model and the nature of the driving cycle. Performance requirements have been published by the United States Council for Automotive Research (USCAR) [2,3]. The requirements set maximum charge and discharge powers at the battery leads and energy requirements that depend on the vehicle configuration. It is expected that when the driving cycle demands (or delivers) more power from the battery than the guidelines specify, the internal combustion engine (ICE) will make up the difference (or the energy will be rejected as braking heat). A generic protocol has been developed by USCAR, called the hybrid pulse-power capability (HPPC) protocol, to help developers assess the ability of a cell to meet the pulse-power and energy goals [4]. The combined model we develop in this work allows us to determine the utility and limitations of the HPPC protocol.

We initiated this study because a claim is made that a flat-potential system would lead to a larger capacity usage [5]. Thus, one

Abbreviations: Gr, Li_xC_6 electrode; HEV, hybrid electric vehicle; HPPC, hybrid pulse-power characterization; ICE, internal combustion engine; LFP, Li_yFePO_4 electrode; LMS, $Li_{y+0.16}Mn_{1.84}O_4$ electrode; LTO, $Li_{4+3x}Ti_5O_{12}$ electrode; PHEV, plug-in hybrid electric vehicle; SEI, solid–electrolyte interphase; SOD, state-of-discharge.

* Corresponding author. Tel.: +1 510 643 1972; fax: +1 510 642 4778.
E-mail addresses: albertus@berkeley.edu (P. Albertus), jc.puravida@gmail.com (J. Couts), vsrinivasan@lbl.gov (V. Srinivasan), newman@newman.cchem.berkeley.edu (J. Newman).

0378-7753/$ – see front matter © 2008 Elsevier B.V. All rights reserved.
doi:10.1016/j.jpowsour.2008.05.012

Nomenclature

a	vehicle acceleration ($m\,s^{-2}$)
a	specific area ($m^2\,m^{-3}$)
A_{sep}	separator area (m^2)
A_{surf}	front cross-sectional area of the vehicle (m^2)
c	concentration ($mol\,m^{-3}$)
D	diffusion coefficient ($m^2\,s^{-1}$)
E	energy (J)
F	Faraday's constant (96,487 $C\,mol^{-1}$)
g	gravitational acceleration ($m\,s^{-2}$)
i	current density ($A\,m^{-2}$ superficial)
j_{insert}	pore wall flux for insertion reaction ($mol\,m^{-2}$ interfacial)
m_{batt}	mass of battery (cell basis) (kg)
$m_{passengers}$	mass of passengers (kg)
$m_{vehicle}$	total vehicle mass (kg)
P	power required at the wheels (W)
P_{max}	maximum power (W)
Q	specific capacity ($Ah\,m^{-2}$)
r	radius (m)
r_{air}	air drag coefficient
r_{roll}	rolling resistance
R	resistance (Ω)
t_+	transference number of Li^+
U	equilibrium potential (V)
v	vehicle velocity ($m\,s^{-1}$)
V_{max}	upper cutoff potential (V)
V_{min}	lower cutoff potential (V)

Greek letters

α	transfer coefficient
ε	volume fraction
η_s	surface overpotential, $\phi_1 - \phi_2 - U$ (V)
κ	conductivity ($S\,m^{-1}$)
ρ_{air}	density of air ($kg\,m^{-3}$)

Superscripts and subscripts

1	solid phase
2	liquid phase

goal of this work is to assess the validity of this claim. Other goals include using the basic insights of the simple model to elucidate the results of the combined model, and improving the understanding of the performance of different cell chemistries.

1.1. Previous research

Fellner and Newman completed a study of battery sizing and capacity utilization for hybrid electric vehicles. Key findings of their work include that for a HEV application less than 5% of the capacity of the battery is used during a standard driving cycle [6,7]. These authors used a combined vehicle and battery model; the model used a varying battery weight, and hence vehicle weight. The authors performed separate optimizations for maximum mileage and minimum battery size, and found the resulting separator areas to be very similar. In their study the battery weight ranged from 62.0 to 112.8 kg, and the thickness of the cell sandwich was around 425 μm, not including current collectors. The chemistry studied in their work was Li_xC_6 *vs.* $Li_yMn_2O_4$. Their Li_xC_6 electrode was amorphous carbon, and had an equilibrium potential with a steady slope from 0 to *ca.* 1.0 V. The authors did not consider the effect of cell chemistry on their results, nor did they extend their study to PHEVs, which have received attention only in the past few years. These authors assumed that the ICE would operate at a constant load, and the battery would provide all the load-leveling. This accounts for the very large batteries they found (for comparison, the weight of the modules in the Prius is around 29 kg). Our approach in this work is different in two ways. First, we optimize our electrode thicknesses for a given power-to-energy ratio (resulting in cell sandwiches between 150 and 265 μm, depending on chemistry and vehicle configuration), while Fellner and Newman arbitrarily chose the thickness of their cell sandwich. Second, our power management routine limits the power at the battery leads and assumes that both the battery and ICE assist with load-leveling. As our results show, these two differences lead to an order-of-magnitude reduction in battery size and weight, which is much more realistic for the systems being designed today.

We were unable to find any literature references on the effect of cell chemistry on battery utilization and sizing, but we did find a number of works discussing battery requirements for hybrid and plug-in hybrid vehicles [7–13]. In the two most important papers on this topic, Markel and Simpson discuss the possible operating concepts for grid-charged hybrid electric vehicles (which we denote as PHEVs) [8,9]. These authors argue that if an initial all-electric range is included, the battery must be sized to meet the peak power requirement of the driving cycle, while if the ICE is turned on during high-power-requirement segments, the maximum required power can be reduced by the amount of power supplied by the ICE. Rather than an all-electric mode followed by a HEV mode, the authors advocate the use of a "blended strategy" in which the ICE and battery work together to meet the power demands of the driving cycle at all times. Figs. 10 and 11 of Kelly et al. clearly depict the difference between the two strategies [14]. The blended strategy, rather than an all-electric range followed by a HEV range, should be considered as the expected development pathway for PHEVs, and is the one we use in our model [15].

Other relevant work reports on direct testing of capacity usage in the batteries of the Toyota Prius and Honda Insight. Kelly et al. connected a 2000 model year Honda Insight and a 2001 model year Toyota Prius to a chassis dynamometer and measured the state-of-discharge during a variety of driving segments [14]. They found that the Insight limited the capacity usage to a maximum of 60% of the rated capacity, while the Prius limited it to 40%. While the Prius used an algorithm to return the state-of-discharge (SOD) to approximately 45%, the Insight did not have a target SOD to which the control system actively returned the battery. However, while the SOD could range by up to 40% (Prius) or 60% (Insight), during normal use it varied by only a few percent. The larger SOD range occurred only when the dynamometer was used to simulate a large incline or decline.

As a final important point from the literature, Nelson notes that the state-of-charge window during normal operation influences the cycle life of the cell, although he does not provide quantitative information of this effect [13].

2. Cell chemistry details

In this section we describe the features of the cell chemistries we chose for the present study: a $Li_xC_6/Li_{y+0.16}Mn_{1.84}O_4$ cell with both normal and artificially flat equilibrium potentials, and a $Li_{4+3x}Ti_5O_{12}/Li_yFePO_4$ cell. The $Li_xC_6/Li_{y+0.16}Mn_{1.84}O_4$ cell represents a relatively high-potential/high-resistance cell, while the $Li_{4+3x}Ti_5O_{12}/Li_yFePO_4$ cell represents a relatively low-potential/low-resistance cell.

Table 1
Equilibrium potential equations

Electrode	Equilibrium potential (*vs.* Li/Li$^+$, V)
Li_xC_6	$U = 0.124 + 2.5\exp(-70x) + 0.0351\tanh\left(\frac{x-0.286}{0.083}\right) - 0.0045\tanh\left(\frac{x-0.9}{0.119}\right) - 0.035\tanh\left(\frac{x-0.99}{0.05}\right) - 0.0147\tanh\left(\frac{x-0.5}{0.034}\right) - 0.102\tanh\left(\frac{x-0.194}{0.142}\right) - 0.022\tanh\left(\frac{x-0.98}{0.0164}\right) - 0.011\tanh\left(\frac{x-0.124}{0.0226}\right) - 0.0155\tanh\left(\frac{x-0.105}{0.029}\right)$
Li_xC_6, artificially flat	$U = 0.14 + 2.5\exp(-70x) - \exp(50(x-1.04))$
$Li_{y+0.16}Mn_{1.84}O_4$	$U = 4.1375 + \frac{0.08}{\ln 10}\ln\frac{550.0001 - 550((y-0.45)/0.55)}{550((y-0.45)/0.55)+1} - 0.1375\left(\frac{y-0.45}{0.55}\right) + \exp\left(500\left(0.01 - \left(\frac{y-0.45}{0.55}\right)\right)\right)$
$Li_{y+0.16}Mn_{1.84}O_4$, artificially flat	$U = 4.055 + \exp(50(-0.01 - x)) - \exp(50(x-1.023))$
Li_yFePO_4	$U = 3.5796 + 0.55163\,\mathrm{atan}(23.54 - 408.95y) + 0.46309\,\mathrm{atan}(-203.36y + 202.43)$
$Li_{4+3x}Ti_5O_{12}$	$U = 2.8441 - 1.3368x + 0.40438\exp(-253.88x) - 0.14647\tanh(36.507(x-0.03346)) - 0.0015515\tanh(309.09(x-0.7982)) - 0.76112\tanh(79.778(x-0.8658)) + (1.906 - 1.3224x)\tanh(79.554(x-0.86628))$

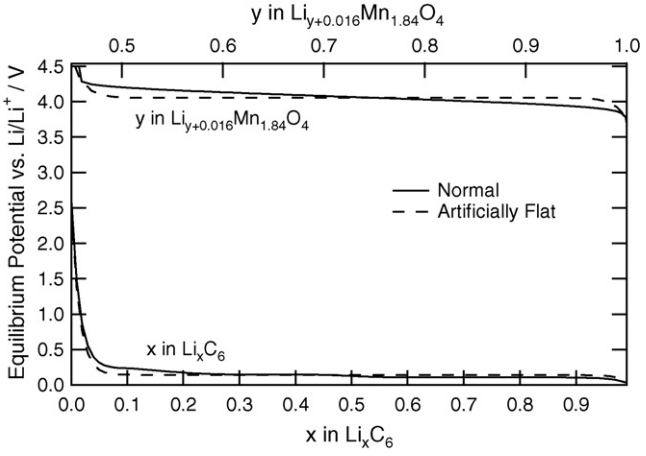

Fig. 1. Normal and artificially flat equilibrium potential curves of the $Li_xC_6/Li_{y+0.16}Mn_{1.84}O_4$ system.

2.1. Equilibrium potential curves

Our equilibrium potential equations are summarized in Table 1. The curves for Li_xC_6, $Li_{4+3x}Ti_5O_{12}$ and $Li_{y+0.16}Mn_{1.84}O_4$ are based on those reported by Christensen et al. [16]. The curve for Li_yFePO_4 is from Srinivasan [17]. We slightly modified a few of these curves to improve convergence of the battery model. Figs. 1 and 2 show plots of these functions.

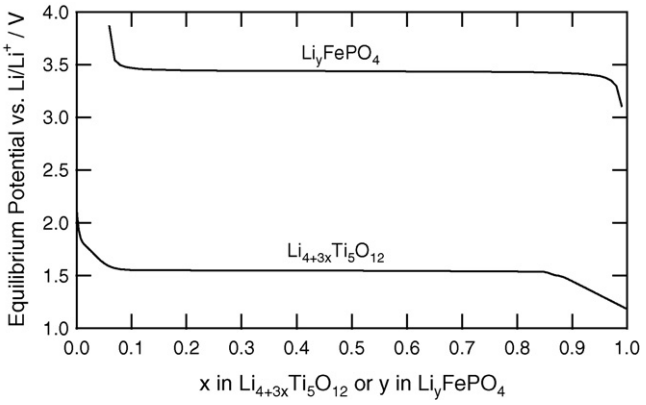

Fig. 2. Equilibrium potentials of the $Li_{4+3x}Ti_5O_{12}/Li_yFePO_4$ system.

2.2. Cell properties and parameters

The cell properties and parameters are summarized in Table 2, which includes an indication of the source where appropriate. We set the capacity ratio of the $Li_xC_6/Li_{y+0.16}Mn_{1.84}O_4$ cells to 1.1:1 and assume a first-cycle capacity loss of 10%, which should be applicable for a synthetic graphite. The combination of this capacity ratio and first-cycle capacity loss implies that the maximum value of x for the Li_xC_6 electrode is 0.809. We use an anode film resistance of 0.005 $\Omega\,m^2$ for the Li_xC_6 electrode, which results in a cell impedance of approximately 20 $\Omega\,cm^2$, a reasonable value for current state-of-the-art graphite-based cells. Because the potential of the $Li_{4+3x}Ti_5O_{12}$ electrode is above the potential at which SEI formation occurs, we use a capacity ratio of 1:1 and assume that there is no first-cycle capacity loss. The volume fraction of inert in each electrode is kept constant relative to the volume fraction of active material. We use a ratio of 1.68:1 active-to-inert for Li_xC_6 and $Li_{4+3x}Ti_5O_{12}$ and 2.22:1 active-to-inert for $Li_{y+0.16}Mn_{1.84}O_4$ and Li_yFePO_4. The remaining cell properties come from the references specified in Table 2, or are set to values deemed representative for current state-of-the-art cells.

The electrode thicknesses and liquid-phase porosities come from optimizing the cells for a given power-to-energy ratio set in the goals given by USCAR [2,3]. We use the HPPC method to determine the usable energy as a function of discharge power, and vary the electrode thicknesses and porosities to maximize the energy and power, while holding the capacity ratio and power-to-energy ratio constant. This method is described in the USCAR manual and by Stewart et al. [4,18]. We optimize HEV cells for a power-to-energy ratio of 83.3:1, and PHEV cells for a power-to-energy ratio of 13:1. The power-to-energy ratio for a PHEV will depend on its intended all-electric range; the value of 13:1 used here is for a PHEV with an intended range of 16 km. For simplicity, we do not repeat the optimization for electrode thicknesses and porosities for each range. We simulated the HPPC tests at a 10*C* rate for discharge and 7.5*C* for charge, with the capacity based on that available at the 1*C* rate.

We present a sample of our optimization results in Fig. 3, which shows the ten-second pulse resistance for the $Li_xC_6/Li_{y+0.16}Mn_{1.84}O_4$ system with both normal and flat discharge curves, and in Fig. 4, which shows the ten-second pulse resistance for the $Li_{4+3x}Ti_5O_{12}/Li_yFePO_4$ system. There are two lines for each system because a separate calculation is made for the charge and discharge resistance. The resistance for the flat potential is slightly lower than for the normal potential in Fig. 3 because a sloped equilibrium potential increases the pulse voltage change

Table 2
Cell properties and parameters

Design-adjustable parameters	Li_xC_6	$Li_{y+0.16}Mn_{1.84}O_4$	$Li_{4+3x}Ti_5O_{12}$	Li_yFePO_4
HEV				
Electrode thickness (μm)[a]	44.6	80	66.1	70
Volume fraction electrolyte[a]	0.33	0.3	0.27	0.34
Volume fraction inert filler[b]	0.250	0.217	0.272	0.205
PHEV				
Electrode thickness (μm)[a]	97.1	175	118	125
Volume fraction electrolyte[a]	0.303	0.275	0.25	0.32
Volume fraction inert filler[b]	0.260	0.225	0.280	0.211

Electrode parameters	Li_xC_6	$Li_{y+0.16}Mn_{1.84}O_4$	$Li_{4+3x}Ti_5O_{12}$	Li_yFePO_4
Diffusion coefficient in solid ($m^2\,s^{-1}$)	9.0×10^{-14}	2.5×10^{-15}	6.8×10^{-15}	3.8×10^{-19}
Film resistance ($\Omega\,m^2$)	0.005	0	1×10^{-5}	1.0×10^{-5}
Reaction rate constant ($mol\,m^{-2}\,s^{-1}$)	1×10^{-3}	5×10^{-12}	3×10^{-3}	5×10^{-14}
Average particle radius (μm)	5	1.75	0.1	0.02
Current collector thickness (μm)	7.5 (copper)	12.5 (aluminum)	7.5 (aluminum)	12.5 (aluminum)
Theoretical specific capacity ($mAh\,g^{-1}$)	372	154	175	170
Densities ($g\,cm^{-3}$)	2.27	4.40	3.50	3.60
Matrix conductivity ($S\,m^{-1}$)[c]	100	100	100	100

Cell sandwich parameters	$Li_xC_6/Li_yMn_2O_4$ electrode pair	$Li_{4+3x}Ti_5O_{12}/Li_yFePO_4$ electrode pair
Separator thickness (μm)	25	25
Cell sandwich mass ($kg\,m^{-2}$)		
HEV	0.440	0.411
PHEV	0.822	0.727
Cell sandwich capacity ($Ah\,m^{-2}$)		
HEV	12.7	18.5
PHEV	28.7	34.1

Parameter	
Initial salt concentration, $LiPF_6$ in EC:DMC (M)	1.0
Densities ($g\,cm^{-3}$)	
Inert filler	1.855
Electrolyte	1.2
Separator material	0.9
Aluminum	2.71
Copper	8.95

[a] Optimized.
[b] Set value (see text).
[c] Set to arbitrarily high value.

used to calculate the resistance. The resistance is relatively flat in the SOD range from 0.2 to 0.8, but increases quickly outside that range due to a more rapidly changing equilibrium potential and solid-phase diffusion limitations. The resistance reflects the shape of the equilibrium potentials in other ways as well; for example, in Fig. 3, the slight rise in the SOD around 0.4 is due to the change in slope of the equilibrium potential of the Li_xC_6 electrode in that range. Finally, the resistance of the $Li_{4+3x}Ti_5O_{12}/Li_yFePO_4$ system is lower than the $Li_xC_6/Li_{y+0.16}Mn_{1.84}O_4$ system because the potential of the $Li_{4+3x}Ti_5O_{12}$ electrode is above the potential at which SEI

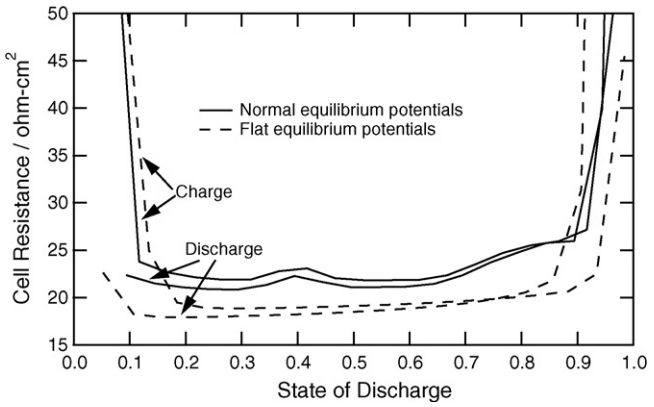

Fig. 3. Ten-second pulse resistance of the $Li_xC_6/Li_{y+0.16}Mn_{1.84}O_4$ system, with normal and artificially flat equilibrium potential curves and the HEV cell parameters. The resistance was calculated using the HPPC method.

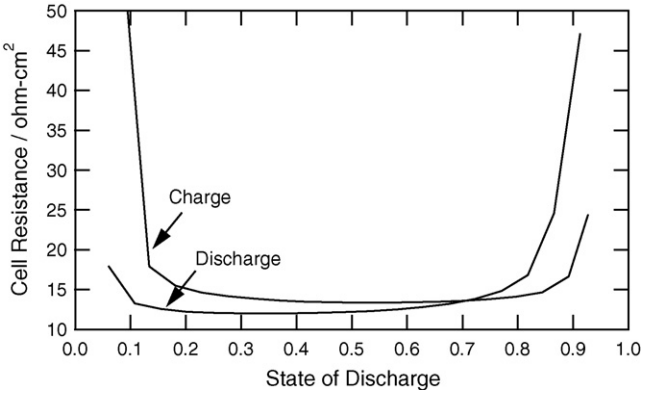

Fig. 4. Ten-second pulse resistance of the $Li_{4+3x}Ti_5O_{12}/Li_yFePO_4$ system with the HEV cell parameters. The resistance was calculated using the HPPC method.

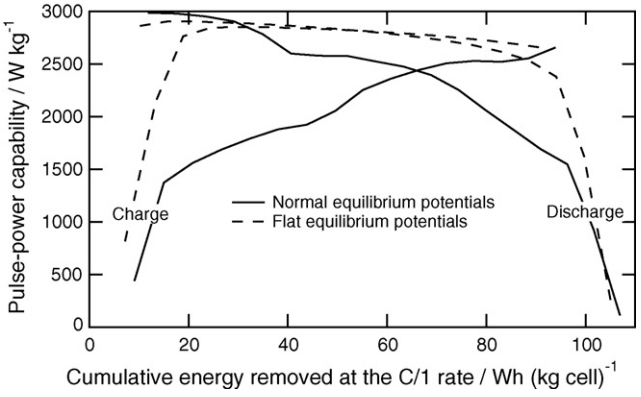

Fig. 5. Discharge and charge pulse-power for the $Li_xC_6/Li_{y+0.16}Mn_{1.84}O_4$ system with the HEV cell parameters as a function of the cumulative energy removed at the *C*/1 rate. The charge pulse-power displayed here has been divided by 0.8 according to the USCAR manual.

formation occurs, which leads to a lower film resistance and the ability to use smaller particles.

Important parameters required for the HPPC method are the upper and lower cutoff potentials. In the case of the $Li_xC_6/Li_{y+0.16}Mn_{1.84}O_4$ system, the upper cutoff is limited by the stability of the electrolyte; we use a value of 4.35 V. The lower cutoff is typically set to 55% of the upper cutoff, which we do for the $Li_{4+3x}Ti_5O_{12}/Li_yFePO_4$ system, but for the $Li_xC_6/Li_{y+0.16}Mn_{1.84}O_4$ system we set the lower cutoff potential to 3.2 V because of stability limits of the $Li_{y+0.16}Mn_{1.84}O_4$ electrode. For the $Li_{4+3x}Ti_5O_{12}/Li_yFePO_4$ system, the upper cutoff potential is not constrained by material stability; we use a value of 2.215 V, which we adjusted until the discharge and regeneration curves crossed at a SOD of approximately 0.5.

Fig. 5 shows the discharge and charge pulse-power as a function of SOD for the $Li_xC_6/Li_{y+0.16}Mn_{1.84}O_4$ system with both a flat and sloped equilibrium potential for the HEV cell parameters. The pulse-power at which the charge and discharge curves cross is the maximum pulse-power at which the cell could be operated, assuming that both the discharge and charge pulse-power goals must be satisfied. Note that the pulse-power curves are much flatter in the case of the flat equilibrium potential. Fig. 6 shows a similar plot for the $Li_{4+3x}Ti_5O_{12}/Li_yFePO_4$ system; again, the pulse-power curves are relatively flat.

The usable energy is defined as the amount of energy available between the discharge and charge pulse-power curves for a given pulse-power. For example, at a pulse-power of 1500 W kg^{-1} and

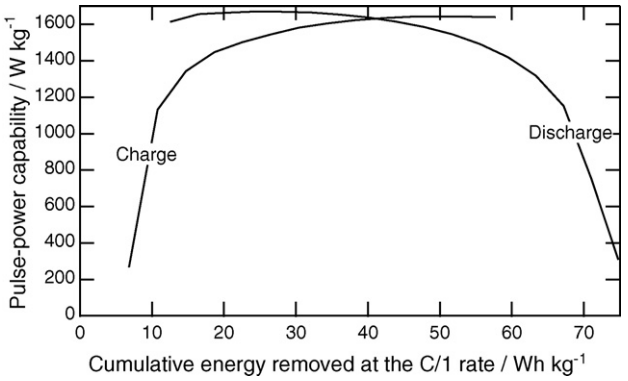

Fig. 6. Discharge and charge pulse-power for the $Li_{4+3x}Ti_5O_{12}/Li_yFePO_4$ system with the HEV cell parameters as a function of the cumulative energy removed at the *C*/1 rate. The charge pulse-power displayed here has been divided by 0.8.

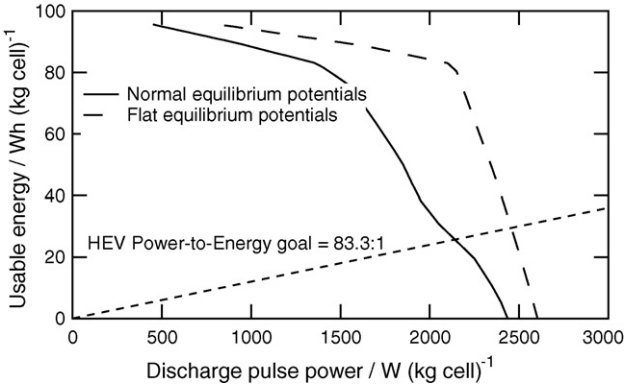

Fig. 7. Usable energy as a function of discharge pulse-power for the $Li_xC_6/Li_{y+0.16}Mn_{1.84}O_4$ system with the HEV cell parameters, for both normal and artificially flat equilibrium potential curves.

the normal equilibrium potential curve shown on Fig. 5, the usable energy is around 75 Wh kg^{-1}. Fig. 7 shows the usable energy as a function of discharge pulse-power for the flat and normal equilibrium potentials for the $Li_xC_6/Li_{y+0.16}Mn_{1.84}O_4$ system. We have also plotted the HEV power-to-energy ratio of 83.3:1 on Fig. 7. To optimize the electrode thicknesses and liquid-phase volume fractions for the HEV application, while holding the capacity ratio constant, we iterated to find the maximum usable energy along the power-to-energy = 83.3:1 line. For the PHEV application we used a ratio of 13:1. Optimization results are given in Table 2.

3. Model description

3.1. Battery model

Our simulations use a novel combined battery and vehicle model. The battery model is Dualfoil, and the vehicle model is based on the one developed by Fellner and Newman [7,19–22]. The Dualfoil program employs porous electrode theory, a macro-homogenous approach to treating the phenomena occurring in the porous electrodes of batteries. The version used in this work has six coupled differential equations (a material balance on the electrolyte, a material balance on the solid intercalant, Ohm's law in the liquid phase, Ohm's law in the solid phase, a current balance that relates the flow of current between the solid and liquid phases, and a Butler–Volmer kinetics expression). These equations are solved numerically and simultaneously at each time step. A summary of the equations is presented in Table 3. We modified the Dualfoil program in order to integrate it with the vehicle model; the major change was to make the time increment of the driving cycle and the time increment of Dualfoil the same. At the very first time step (when the driving cycle begins), the battery is initialized, and at subsequent time steps, the battery is left in its state rather than

Table 3
Equations used in the Dualfoil model

Equation description	Equation
Electrolyte material balance	$\varepsilon_2 \frac{\partial c}{\partial t} = \nabla \cdot (\varepsilon_2 D \nabla c) - \nabla \cdot \left(\frac{i_2(1-t_+^0)}{F} \right)$
Intercalant material balance	$\frac{\partial c_s}{\partial t} = \frac{1}{r^2} \frac{\partial}{\partial r} \left(D_s r^2 \frac{\partial c_s}{\partial r} \right)$
Liquid-phase Ohm's law	$i_2 = -\kappa \nabla \Phi_2 + \frac{2\kappa RT}{F}(1 - t_+^0) \nabla \ln(f_{\pm} c)$
Solid-phase Ohm's law	$i_1 = -\sigma \nabla \Phi_1$
Butler–Volmer insertion kinetics	$j_{\text{insert}} = \frac{i_0}{F} \left[\exp\left(\frac{\alpha_a F}{RT} \eta_s \right) - \exp\left(\frac{\alpha_c F}{RT} \eta_s \right) \right]$
Exchange current density	$i_0 = i_0'(c_s)^{\alpha_c}(c_e)^{\alpha_a}(c_t - c_s)^{\alpha_a}$
Charge conservation	$\nabla \cdot i_2 = aFj_{\text{insert}}$

Table 4
Vehicle specifications

Specification	Units	Value	Description
Vehicle base mass	kg	1200	Similar to a Toyota Prius
Passenger mass	kg	135	Approximate weight of two people
A_{surf}	m^2	1.75	
r_{roll}		0.015	Typical value for automobiles
r_{air}		0.26	Value for the 2007 Toyota Prius
Powertrain efficiency		0.8	Based on reference [7]
Generator efficiency		0.9	Based on reference [7]
Electric motor efficiency		0.9	Based on reference [7]
Maximum regenerative braking		0.5	Amount of power available for battery charging relative to the total available power

being re-initialized. We discretized the driving cycle into increments of 0.25 s, and therefore the Dualfoil program is called every 0.25 s. The frequency can be increased to improve accuracy. The battery is operated in the constant-power mode.

3.2. Vehicle model

The vehicle model calculates the power required at the wheels at each time step, and takes into account wind resistance, rolling resistance, and acceleration. Table 4 lists the vehicle specifications. Eq. (1) describes how we find the power at each point in the driving cycle,

$$P = 0.5\rho_{air}A_{surf}r_{air}v^3 + m_{vehicle}va + r_{roll}m_{vehicle}gv. \quad (1)$$

The mass of the vehicle is given by

$$m_{vehicle} = m_{base} + m_{passengers} + 1.5A_{sep}m_{batt}. \quad (2)$$

The factor of 1.5 in Eq. (2) accounts for the balance of system above the cell level. From Eqs. (1) and (2) it should be apparent that the battery size affects the power required at the wheels. Once the power at the wheels is determined, we use a simple algorithm to divide the power supply between the ICE and battery. For the HEV configuration, we assume that the ICE runs at a constant value (that denoted by "Base Engine Size" in Table 6) unless the power demanded at the wheels exceeds the power available from the battery, in which case the ICE meets the difference. Thus, the ICE is always on except when the vehicle is braking, in which case it is turned off. In this scheme, the battery serves as the load-leveling device up to its power limit, after which the ICE assists with the load-leveling. For the PHEV configuration, the ICE remains off unless the battery cannot supply the power demanded by the vehicle. The power from the ICE can go either to the battery through the generator or to the wheels through the powertrain (note that for the PHEV configuration no power from the ICE is routed to the battery during the charge-depleting mode). When power is required from the battery, it goes through the electric motor and the powertrain. Power to the battery can come either from the engine, in which case it runs through the generator, or from the wheels, in which case it runs through the powertrain and the generator. In practice, the power management system of a vehicle is much more sophisticated than this simple approach; we believe that this rough approximation is sufficient for the present purposes. Because we allow the power supplied by the ICE to vary, and the efficiency of an ICE depends on its load profile, the calculation of the fuel economy becomes much more difficult, and we therefore do not report fuel-economy values in this work.

Table 5
Relevant USCAR specifications for the HEV and PHEV configurations

Specification	Units	HEV	PHEV
$P_{max,discharge}$	kW	25	45
$P_{max,charge}$	kW	20	30
$C/1$ energy over range in which power goals are met	Wh	300	Depends on desired PHEV range

3.3. HEV configuration

The HEV driving cycle must be charge-neutral, which means that the final state-of-charge must be the same as the initial state-of-charge. In addition, the cell voltage must remain within the specified cutoff potentials. If the cell voltage goes outside the voltage bounds, the separator area is increased (a resolution of 0.1 m^2 is used). If the final state-of-charge does not match the initial state-of-charge, the size of the engine is adjusted. In practice, this can be considered an optimization that results in a minimum separator area. For the HEV configuration, the battery starts and ends at around 50% SOD. The power requirements for the HEV and PHEV configurations are given in Table 5.

3.4. PHEV configuration

In the PHEV configuration the vehicle is charge-depleting rather than charge-neutral. As such, the SOD increases during the driving cycle. In this configuration a separator area is chosen, and the vehicle runs through the driving cycle until the lower cutoff potential is reached. The initial SOD is set as low as possible without the upper cutoff potential being reached during a charging segment. The ICE remains off unless the battery is unable to supply the power required by the driving cycle. Because the ICE supplements the battery during times of high power demand, it is necessary to define equivalent-electric miles rather than all-electric miles. To calculate the equivalent-electric kilometers, we calculate the distance traveled by the vehicle during its driving cycle, and the net energy that it requires. The net energy calculation includes regenerative braking, which we assume captures 50% of the energy available during braking. From these numbers we calculate an energy requirement per kilometer. Next, we calculate the net energy removed from the battery during the driving cycle. Note that this calculation includes the energy returned to the battery during the braking stages; this is necessary to calculate an energy-limited asymptote based on the total energy available in a battery. We found that if no regenerative braking is used in the calculation of the amount of energy required per kilometer traveled, the equivalent-electric range drops by *ca.* 25%. This choice of how to define the equivalent-electric kilometers has the disadvantage that the reported range is dependent on the fraction of regenerative braking, but has the advantage that it will give a more realistic estimate of the distance a PHEV can travel. Also note that this method accounts for the battery efficiency as well as the effect of the battery weight on vehicle weight and hence vehicle efficiency because it treats the energy flow at the battery leads. For reference, the energy requirement of our vehicles is in the range of 118–132 Wh km^{-1}. As shown in Table 5, we set the maximum discharge power from the battery (at the leads) to 45 kW, and the maximum charge power (at the leads) to 30 kW.

3.5. Driving cycle

We use a single driving cycle in this work, based on the urban driving cycle shown in Fig. 1 of Fellner and Newman [7]. The driving cycle we use is shown in Fig. 8. The cycle is composed of six 1-min cycles and has three 10-s accelerations, two 12-s accelerations, and

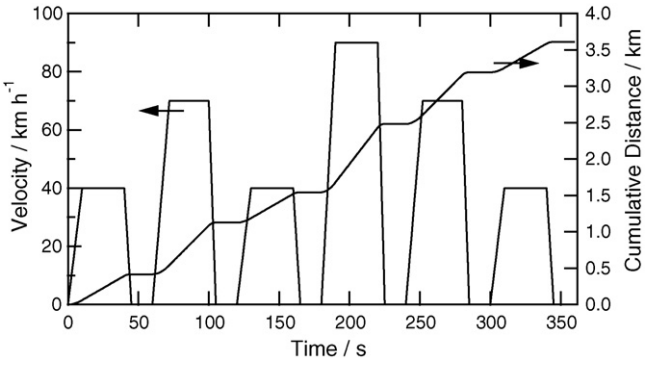

Fig. 8. Driving cycle used in both HEV and PHEV simulations. The driving cycle is composed of six 1-min cycles, and has three 10-s accelerations, two 12-s accelerations, and one 15-s acceleration. The braking segments are 5 s, and the rests are 15 s.

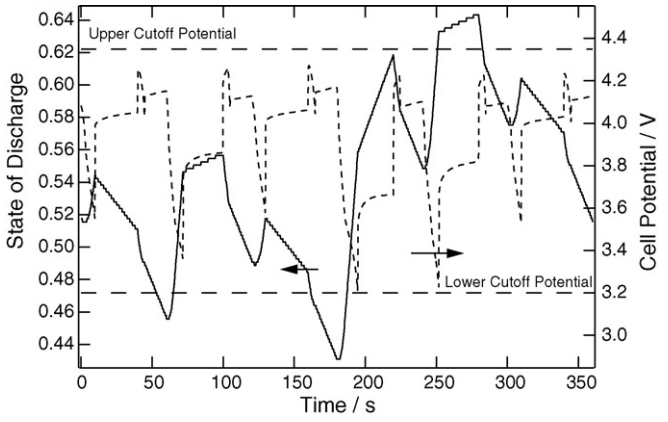

Fig. 9. Performance of the $Li_xC_6/Li_{y+0.16}Mn_{1.84}O_4$ system with a normal equilibrium potential for a HEV driving cycle. For this chemistry the separator area is 14.1 m^2 and the battery mass is 6.2 kg.

one 15-s acceleration. The braking segments are 5 s, and the rests are 15 s. Note that this driving cycle uses a constant acceleration rate. One of the conclusions from Fellner's work is that the precise characteristics of the driving cycle are relatively unimportant provided that it contains essential features such as rapid braking and acceleration segments. In practice, it is the high-power peaks that determine battery sizing (at least for HEVs). We explored different driving cycles and found that the presence of high-power spikes, as well as long charge or discharge segments, can have a significant influence on battery capacity usage. For example, a charge-neutral HEV driving cycle that involves going up and down a large hill may use a larger fraction of the battery capacity than an aggressive urban cycle primarily composed of high-power spikes. Thus, our results for battery usage should be taken in the context of the driving cycle we have chosen.

3.6. Model limitations

There are several model limitations, including those related to the battery model and those related to the vehicle model. A main assumption of the battery model relevant to the present purpose is isothermal operation; in practice we expect the battery temperature in a HEV or PHEV to depend on the cycling history and ambient temperature. A good cooling system limits the error introduced by this assumption [23,24]. The category of vehicle-level limitations includes the fact that driving time is cut into segments of 0.25 s and a simplified power-allocation routine is used. There is also the assumption of constant-thickness electrodes for the PHEV application; in practice we would expect there to be an optimum based on the power-to-energy ratio of the particular PHEV battery under consideration. Finally, because we use a variable-load ICE, we do not calculate fuel economy; in general the efficiency of an ICE strongly depends on the load and load variation.

4. Results and discussion

4.1. HEV simulations and analysis

Fig. 9 shows the results of the HEV simulations for the $Li_xC_6/Li_{y+0.16}Mn_{1.84}O_4$ system with normal equilibrium potentials. The figure shows that the HEV cycle is charge-neutral, and that the convergence routine ensures that the cell potential comes very close to touching the lower cutoff potential. The performance of the $Li_xC_6/Li_{y+0.16}Mn_{1.84}O_4$ system with artificially flat equilibrium potentials and the $Li_{4+3x}Ti_5O_{12}/Li_yFePO_4$ system are qualitatively similar to the results in Fig. 9 and are therefore omitted. Table 6 presents the results for all three of the chemistries. For the $Li_xC_6/Li_{y+0.16}Mn_{1.84}O_4$ system, the separator area is similar for the regular and artificially flat equilibrium potentials. The difference is due to the fact that the flat potential allows for a slightly larger battery utilization, and therefore a smaller separator size can be used, though the difference is relatively small (around 5%). The SOD range used by the $Li_xC_6/Li_{y+0.16}Mn_{1.84}O_4$ system (in the 20–25% range) is much larger than that found by Fellner and Newman; as explained before, this is a result of the much smaller battery size, which is related to the much thinner, optimized cell sandwich, and the "blended" operating strategy. The separator area for the $Li_{4+3x}Ti_5O_{12}/Li_yFePO_4$ system is substantially larger than for the $Li_xC_6/Li_{y+0.16}Mn_{1.84}O_4$ system. In order to understand this difference, it is important to consider the value of $(U - V_{min})V_{min}/R$, where V_{min} is the lower cutoff potential and R is the area-specific cell resistance. This is what is plotted in Figs. 5 and 6, which show the pulse-power capability of the $Li_xC_6/Li_{y+0.16}Mn_{1.84}O_4$ system is substantially higher than that of the $Li_{4+3x}Ti_5O_{12}/Li_yFePO_4$ system.

The batteries here are smaller than what would be expected for a commercial application; these results should be interpreted as a minimum separator area size. In practice, larger batteries are

Table 6
Performance results for the HEV driving cycle

Electrode system	Combined model results					Simple model results	
	Base Engine Size (kW)	SOD range (%)	Separator area (m^2)	Battery mass (cell level) (kg)	Battery efficiency (%)	Separator area (m^2)	Battery mass (cell level) (kg)
$Li_xC_6/Li_{y+0.16}Mn_{1.84}O_4$ (regular equilibrium curves)	16.08	21.24	14.1	6.20	92.50	24.2	10.64
$Li_xC_6/Li_{y+0.16}Mn_{1.84}O_4$ (flat equilibrium curves)	15.90	22.27	13.5	5.93	93.22	19.8	8.70
$Li_{4+3x}Ti_5O_{12}/Li_yFePO_4$	17.32	17.44	27.4	11.27	86.7	38.2	15.71

required because the performance goals are for end-of-life and battery performance declines with cycling and time. Thus, a battery that initially exceeds the requirements needs to be installed. Also, the USCAR HEV goals have an energy requirement in addition to a pulse-power requirement. The energy requirement is for 300 Wh over the SOD range over which the pulse-power goals are satisfied. A larger energy requirement allows the battery to deliver energy during a long uphill or capture energy during a long downhill; in practice this 300 Wh goal represents a tradeoff between vehicle efficiency and battery size. We refrain from speculating on whether the 300 Wh energy goal is a good one; it is primarily related to the vehicle efficiency and the expected driving cycle.

Fig. 5 shows that, when operated at a low rate, at the cell level *ca.* 110 Wh kg^{-1} is available from the $Li_xC_6/Li_{y+0.16}Mn_{1.84}O_4$ system with normal equilibrium potentials. For a battery that weighs 6.20 kg at the cell level, around 680 Wh would be available assuming the entire capacity could be used. The driving cycle shown here uses 21.24% of the SOD range, which corresponds to around 144.4 Wh. Noting that the USCAR goal is 300 Wh (over the range where the power goals are met), we can see that the battery would need to be increased in size in order to meet this energy goal. This implies that for the vehicle design, fraction of regenerative braking, and driving cycle we use here, less than 300 Wh is required of the battery. Fig. 5 shows that with artificially flat equilibrium potentials much more energy is available at a high pulse-power than with normal equilibrium potentials, which implies a substantially smaller battery could be used. However, as shown in Table 6, the flat-potential $Li_xC_6/Li_{y+0.16}Mn_{1.84}O_4$ system has only a slightly smaller size and larger capacity usage. We discuss the reason for this in more detail in Sections 4.2 and 4.3.

We have listed the battery efficiencies in Table 6. The USCAR goals have a requirement of 90% round-trip energy efficiency for a 25-Wh cycle. The $Li_xC_6/Li_{y+0.16}Mn_{1.84}O_4$ systems have an overall battery efficiency above 90%, while the $Li_{4+3x}Ti_5O_{12}/Li_yFePO_4$ system has an overall efficiency below 90%. This difference may be at least partly attributable to the fact that the lower cutoff potential for the $Li_xC_6/Li_{y+0.16}Mn_{1.84}O_4$ systems needs to be kept relatively high (at 3.2 V) because of stability considerations. In any case, all of these systems would have an efficiency above 90% for the driving cycle used here if they were sized for end-of-life requirements and were required to meet a higher energy requirement.

We also list results from the simple model (Eq. (2) of reference [1]) in Table 6. In order to obtain the separator areas for the simple model, we used the ten-second pulse resistances shown in Figs. 3 and 4 at the 50% SOD mark. We imposed no energy requirement for the simple model so the results shown in Table 6 are a minimum separator area size (with a SOD range, and hence energy, of 0). Here we see that for all systems the area given by Eq. (2) of the companion paper is larger than the area calculated by our combined model. Given that Eq. (2) should provide a lower limit on the separator area, this result requires further study. Note that Eq. (2) assumes that the battery is a linear system; in practice the resistance (as defined by the HPPC protocol) will depend on the rate as well as the duration of the current pulse. In Fig. 10 we show the ten-second pulse resistance as a function of *C*-rate at the 50% SOD point. Here we see that the resistance falls as the *C*-rate is increased. The fall in the resistance with increasing *C*-rate can be attributed to the Butler–Volmer kinetics, which contains an exponential relationship between current and applied potential. We attempted to calculate the ten-second pulse resistance at rates above 30 C, but the results began to break down; at some point a limiting current is reached. If we used the resistance at the 30 C rate to calculate the areas given in Table 6, we would have found separator areas of 18.7, 16.5, and 27.3 m^2, respectively. We attribute the difference in the areas given in Table 6 for the combined model and simple model

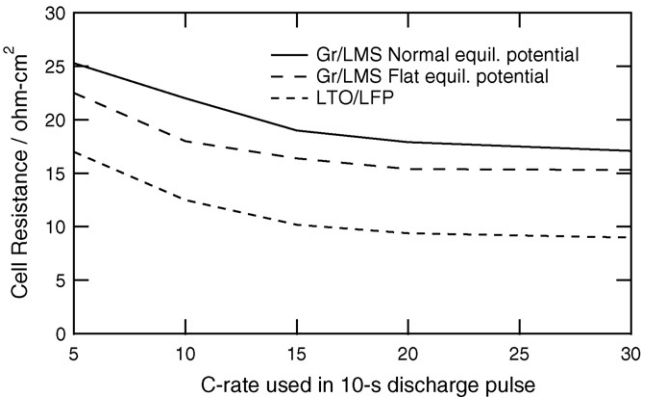

Fig. 10. Ten-second pulse resistance at 50% SOD as a function of *C*-rate for the listed chemistries with HEV cell parameters. Gr = Li_xC_6, LMS = $Li_{y+0.16}Mn_{1.84}O_4$, LTO = $Li_{4+3x}Ti_5O_{12}$, LFP = Li_yFePO_4.

to the fact that the combined battery and vehicle model does not operate like the HPPC protocol (the current in the combined model changes every 0.25 s). We also checked the highest current reached during the HEV simulations for all three chemistries and found that the $Li_{4+3x}Ti_5O_{12}/Li_yFePO_4$ system reaches a *C*-rate of 42.2, and the $Li_xC_6/Li_{y+0.16}Mn_{1.84}O_4$ system reaches a *C*-rate of 43.5 (normal potential) or 45.4 (flat potential). Thus, using the simple model to estimate the size of a battery for a HEV depends on getting an accurate estimate of the battery resistance in its actual operation. Using a resistance calculated with the HPPC protocol, which uses a ten-second pulse at a specified current, may introduce substantial error.

4.2. PHEV simulations and analysis

Fig. 11 shows the cell potential as a function of time for the $Li_xC_6/Li_{y+0.16}Mn_{1.84}O_4$ system with a separator area of 75 m^2 and

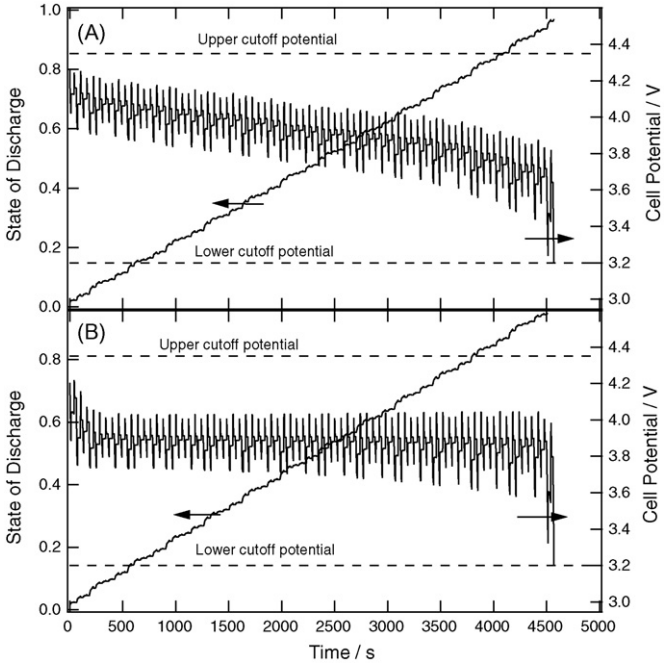

Fig. 11. Performance of the $Li_xC_6/Li_{y+0.16}Mn_{1.84}O_4$, system with a normal (A) and flat (B) potential profile for the PHEV cell parameters and configuration and a separator area of 75 m^2.

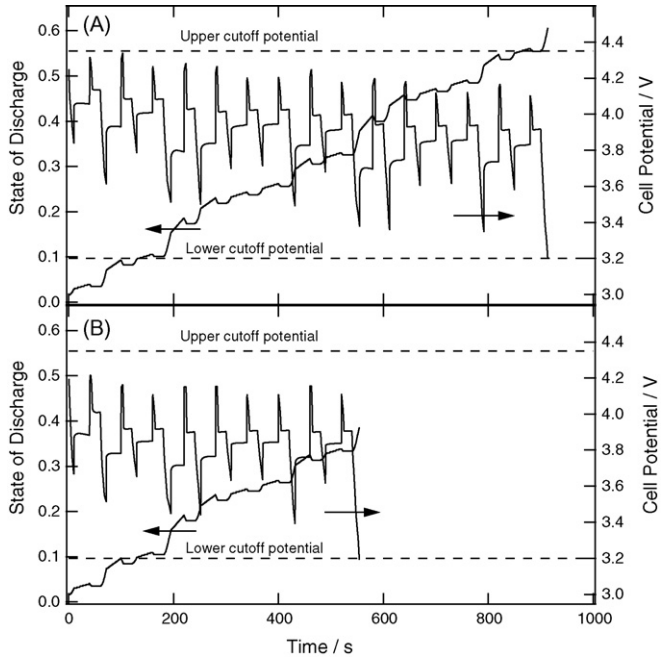

Fig. 12. Performance of the $Li_xC_6/Li_{y+0.16}Mn_{1.84}O_4$ system with a normal (A) and flat (B) equilibrium potential profile for the PHEV cell parameters and configuration and a separator area of 25 m^2.

both the flat and normal equilibrium potential curves. This figure clearly shows the magnitude of the potential spikes, as well as the shapes of the equilibrium potentials. The time at which the lower cutoff potential is reached is very similar for the flat and normal equilibrium potentials; when the potential spikes are small because of a large separator area, very similar performance should be expected from a sloped and artificially flat set of equilibrium potentials, assuming that the cells have the same capacity and average voltage. For the $Li_{4+3x}Ti_5O_{12}/Li_yFePO_4$ system with a separator area of 75 m^2 the voltage spikes are much larger than in Fig. 11, and the time at which the lower cutoff is reached is much earlier. Although a lower resistance permits higher currents for a given voltage drop, the potential of this system is also lower, and the interplay of these effects is roughly captured by Eq. (2) of the companion paper. Fig. 12 shows the cell potential for a smaller separator area (25 m^2) for the $Li_xC_6/Li_{y+0.16}Mn_{1.84}O_4$ systems. Here, we see that the potential spikes are much larger, and the normal equilibrium potential is able to achieve a greater time (distance) before the lower cutoff potential is reached.

In order to help explain why the normal-potential system achieves a greater time, we construct a new kind of plot that can be described as a hybrid between a Peukert and HPPC plot. The goal is to understand the pulse rate capability of the different cell chemistries we are exploring. We show this hybrid plot in Fig. 13. It is constructed by using a HPPC-like protocol in which discharge and charge pulses of a given magnitude (the abscissa in Fig. 13) are applied for 10 s each, separated by a 40 s rest. The SOD is increased in increments of 0.02 with a constant current at the 1 C rate, and the cell is allowed to relax for an hour prior to the application of the next set of discharge and charge pulses. At some point during one of the discharge pulses, the cell reaches the lower cutoff potential, at which point the SOD is recorded and plotted on the ordinate. We can see from Fig. 13 that at *C*-rates in the range from *ca.* 19 to 30 (in the SOD range below *ca.* 0.7), the rate capability of the normal-potential system is greater than the flat-potential system. We attribute this to two independent effects. First, as shown in Fig. 1, the cell potential for the normal-potential system is greater than the flat-potential

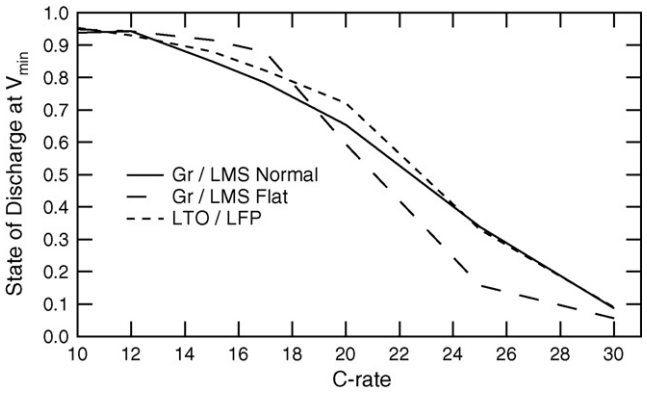

Fig. 13. Hybrid Peukert-HPPC plot showing the SOD at which the lower cutoff is reached as a function of the *C*-rate of the applied pulse for cells with the PHEV parameters. This method starts the cell at a SOD of 0, moves in SOD increments of 0.02 separated by a 1-h rest, and applies a 10-s charge and discharge pulse of equal magnitude separated by a 40-s rest. Gr = Li_xC_6, LMS = $Li_{y+0.16}Mn_{1.84}O_4$, LTO = $Li_{4+3x}Ti_5O_{12}$, LFP = Li_yFePO_4.

system below a SOD of *ca.* 0.5. Second, as we discuss more in Section 4.3, for a flat-potential system that receives consecutive discharge or charge pulses, there will be a build-up and persistence of a solid-phase concentration gradient through the electrode depth. In the SOD range from 0 to 0.5, we would expect superior performance from the normal-potential system due to its higher potential. We attribute its better performance up to a SOD of *ca.* 0.7 in Fig. 13 to the second effect.

By running the PHEV model with a variety of separator areas we can study equivalent-electric distance, separator area, and capacity usage. We show results in Figs. 14 and 15. Here we see that, for a small separator area, the equivalent-electric distance and the capacity usage of the batteries are small. As the size of the battery is increased, the equivalent-electric distance increases at a slope initially lower and then approaching the asymptotic value. The change in slope is also present in Fig. 5 of reference [1]. As explained there, the bend is due to a change in the slope of the pulse-power capability curve, as also seen in Figs. 5 and 6. We have also plotted in Fig. 14, the asymptotes for an energy-limited system given by Eq. (14) of reference [1]. The slopes of the asymptotes and simulation results compare well for the $Li_xC_6/Li_{y+0.16}Mn_{1.84}O_4$ system at distances above *ca.* 35 km, and for the $Li_{4+3x}Ti_5O_{12}/Li_yFePO_4$ system at distances above *ca.* 60 km. As expected, we see that a larger separator area is required for the $Li_{4+3x}Ti_5O_{12}/Li_yFePO_4$ system than for the $Li_xC_6/Li_{y+0.16}Mn_{1.84}O_4$ system as a result of the higher value of $Q\langle V\rangle$ of the latter chemistry. In order to calculate the power- and energy-

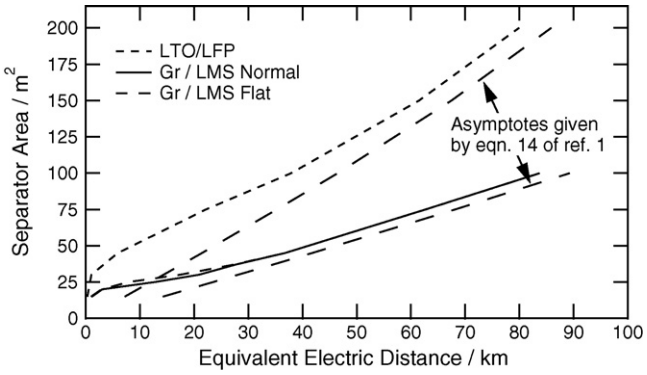

Fig. 14. Equivalent-electric distance of the $Li_xC_6/Li_{y+0.16}Mn_{1.84}O_4$, system and the $Li_{4+3x}Ti_5O_{12}/Li_yFePO_4$ system for a variety of separator areas. Gr = Li_xC_6, LMS = $Li_{y+0.16}Mn_{1.84}O_4$, LTO = $Li_{4+3x}Ti_5O_{12}$, LFP = Li_yFePO_4.

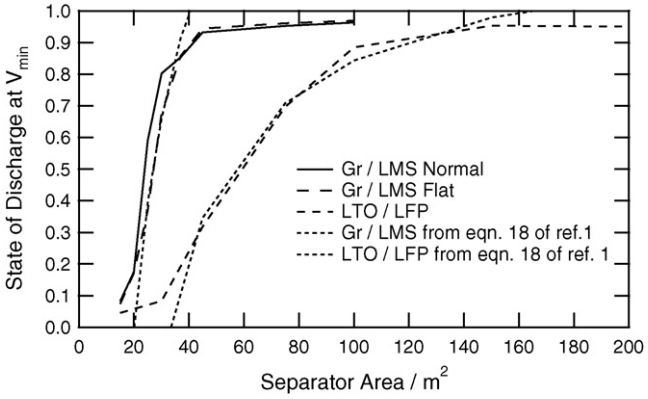

Fig. 15. State-of-discharge at the lower cutoff potential, V_{min}, for the $Li_xC_6/Li_{y+0.16}Mn_{1.84}O_4$ and $Li_{4+3x}Ti_5O_{12}/Li_yFePO_4$ systems for a variety of separator areas. Gr = Li_xC_6, LMS = $Li_{y+0.16}Mn_{1.84}O_4$, LTO = $Li_{4+3x}Ti_5O_{12}$, LFP = Li_yFePO_4.

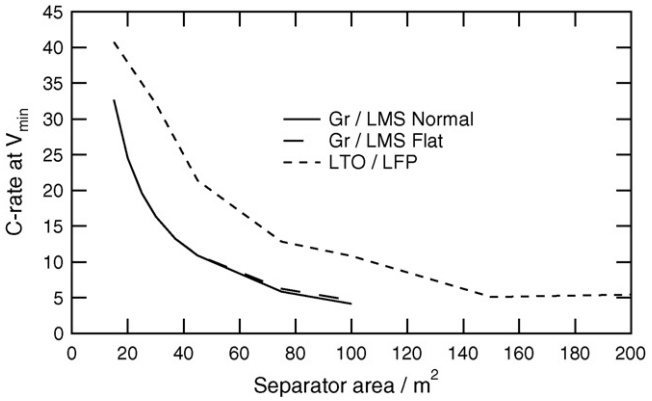

Fig. 16. *C*-rate when the lower cutoff potential, V_{min}, is reached for the $Li_xC_6/Li_{y+0.16}Mn_{1.84}O_4$ system and the $Li_{4+3x}Ti_5O_{12}/Li_yFePO_4$ system. Gr = Li_xC_6, LMS = $Li_{y+0.16}Mn_{1.84}O_4$, LTO = $Li_{4+3x}Ti_5O_{12}$, LFP = Li_yFePO_4.

limited slopes and offsets, we would use Eq. (13) from reference [1]. However, this would require an estimate of the value of *B*, as well as the appropriate value of the resistance, *R*, when the lower cutoff potential is reached. We refrain from doing this because not only is it difficult to find good estimates for *B* and *R*, but the magnitude of the "initial" separator area for a PHEV (the size of the separator area to go a distance of 0 km) is also not well defined. In particular, for a distance less than 3.6 km the lower cutoff potential is reached before the vehicle completes the entire driving cycle.

The simplified model from reference [1] also helps us to better understand the results presented in Fig. 15. Eq. (18) from reference [1] shows the expected dependence of ΔSOD on the separator area, *A*. Note that this equation should be applied only at larger values of the separator area (at values where the capacity usage is well above 0). In order to use this relation, we need a value of *B*. From Figs. 5 and 6, we see there is no linear slope from the power maximum near SOD = 0.5, and we therefore treat *B* as a fitting parameter, with the proviso that its value must be within a reasonable range (between 0 and 1). We found a value of $B = 0.5$ for the $Li_xC_6/Li_{y+0.16}Mn_{1.84}O_4$ system and $B = 0.8$ for the $Li_{4+3x}Ti_5O_{12}/Li_yFePO_4$ system. While attempting to apply Eq. (18) from reference [1], we also found that we needed to use smaller values of the resistance than those given in Figs. 3 and 4. While experimenting with different methods to calculate the resistance, we found that the resistance depends not only on the *C*-rate, as shown in Fig. 10 but also on the duration of the pulse that is used during the resistance calculation. In particular, we found that for a two-second pulse, the resistance was *ca.* 10 Ω cm^2 for the $Li_xC_6/Li_{y+0.16}Mn_{1.84}O_4$ system and *ca.* 6 Ω cm^2 for the $Li_{4+3x}Ti_5O_{12}/Li_yFePO_4$ system at the 30 C rate. The resistance depends on the duration of the pulse because the voltage drop associated with solid-phase and liquid-phase diffusion becomes larger with increasing pulse duration. Again, a limitation of the simplified model is that it assumes a single value of the resistance, which is independent of applied current. While it may be necessary, for the sake of benchmarking, to have a protocol for the determination of the pulse-power and resistance, we have shown that the power capability and resistance may be substantially different for a battery in an application.

When we insert the values for *B* and *R* into Eq. (18) from reference [1], we obtain the curves presented in Fig. 15. We see that the results from the simplified model match the more complex model quite well over the intermediate SOD range (from roughly 0.2 to 0.8). However, at low (<0.2) and high (>0.8) values of the SOD, the results from the simplified model deviate from the results from the combined model. At low values of the SOD, this is due to the fact that the PHEV model is run by changing the separator area rather than the equivalent-electric range. Thus, a separator area can be chosen that results in the cell potential hitting the lower cutoff potential at a very early point in the driving cycle, but this will still result in a nonzero value of ΔSOD (which is why the simulation curves do not terminate directly on the abscissa). At high values of the SOD, the pulse-power curve undergoes a change of shape in which the value of ΔSOD gradually approaches 1.0 as the pulse-power capability approaches 0. Thus, while the results from the simplified model move directly to ΔSOD = 1.0 and flatten out, the results from the combined model deviate from this behavior and approach ΔSOD = 1.0 in a gradual manner.

Figs. 14 and 15 show a superior performance by the normal-potential $Li_xC_6/Li_{y+0.16}Mn_{1.84}O_4$ system over a range of separator areas, although results from the simplified model would suggest that, for a system with a higher value of *B* (a more sloped pulse-power capability), the performance should be worse. Fig. 13 showed that at *C*-rates higher than *ca.* 19 the capacity usage of the normal-potential system is superior; over what range of separator areas are *C*-rates higher than *ca.* 19 achieved in the actual vehicle model? Fig. 16 shows the *C*-rate when the lower cutoff potential is reached for the three systems in our study. This plot shows that for the $Li_xC_6/Li_{y+0.16}Mn_{1.84}O_4$ system the *C*-rate is less than *ca.* 19 for separator areas less than *ca.* 25 m^2. Thus, the effects shown in Fig. 13 can contribute to the superior performance of the normal-potential system over a range of separator areas of practical interest. In the next section we turn to a more detailed analysis of the performance of flat-potential systems.

4.3. Rate performance of flat-potential systems

The question that arises from the consideration of Figs. 5, 14 and 15 is why the $Li_xC_6/Li_{y+0.16}Mn_{1.84}O_4$ system with an artificially flat potential performs in such a similar manner to the system with a normal potential, when the pulse-power capabilities are so different. Note that Fig. 5 is given for a HEV cell design (relatively thin electrodes), while Figs. 14 and 15 are based on the PHEV cell design. The results for the ten-second pulse resistance and pulse-power capability of the $Li_xC_6/Li_{y+0.16}Mn_{1.84}O_4$ system with the PHEV cell parameters are shown in Figs. 17 and 18.

The results in these figures have an important qualitative difference from the results in Figs. 3 and 5; the power capability on discharge is essentially identical for the normal and flat equilibrium potentials, which helps explains the reason that the results in Figs. 14 and 15 are so similar for the $Li_xC_6/Li_{y+0.16}Mn_{1.84}O_4$ system with the two different potential profiles. Why do we see very flat

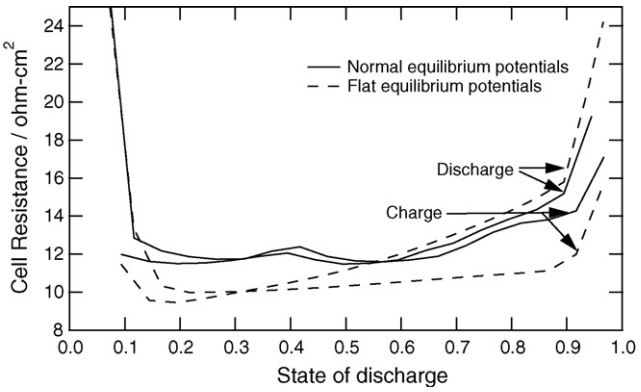

Fig. 17. Ten-second pulse resistance of the $Li_xC_6/Li_{y+0.16}Mn_{1.84}O_4$ system with the PHEV cell parameters. The resistance was calculated using the HPPC protocol.

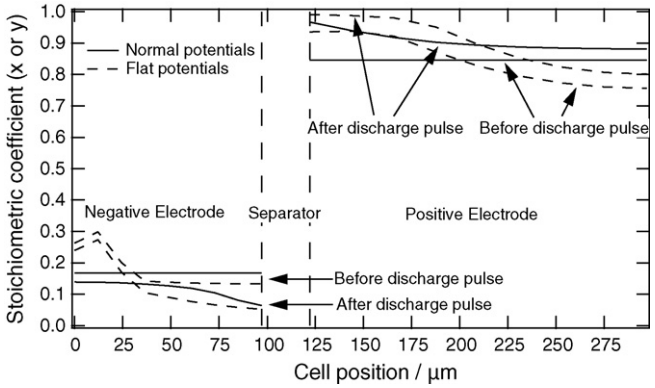

Fig. 19. Internal cell profiles of the stoichiometric coefficient x in Li_xC_6 or y in $Li_{y+0.16}Mn_{1.84}O_4$ immediately before and at the end of a 10*C* discharge pulse at a state-of-discharge of *ca.* 0.8. The results are for the $Li_xC_6/Li_{y+0.16}Mn_{1.84}O_4$ system with the PHEV cell parameters.

pulse-power capability in Fig. 5 and a sloped pulse-power discharge capability in Fig. 18? The PHEV cell design uses thicker electrodes, and during a high-rate pulse will have a more non-uniform current distribution than a HEV cell. This means the region of the electrode near the separator will experience a higher *C*-rate than the same region for a HEV cell design. This is important because it is at these high rates that solid-phase diffusion limitations become significant. In order to explain what is occurring, we plot the detailed profiles within the cell in Fig. 19.

This figure shows an important characteristic of completely flat equilibrium potential cells; without any slope in the potential, there is no driving force for the regions of an electrode to equilibrate to a single composition. Thus, we see that at the end of a 1-h relaxation step following a 1*C* discharge, the flat-potential system still has a higher value of y (and a lower value of x) near the separator/positive electrode interface (and the separator/negative electrode interface). This solid-phase concentration gradient through the depth of the electrode forces current pulses to access the back of the electrode, resulting in more substantial ohmic losses. This is a potential drawback of any flat-potential system. Note that the pulse-power curve on charge is still flat, as shown in Fig. 18, because the step before a pulse charge in the HPPC protocol is a pulse discharge so that concentration gradients that lead to solid-phase diffusion limitations have not been established. Thus, pulse-power performance declines occur when a discharge pulse follows a discharge step, or a charge pulse follows a charge step.

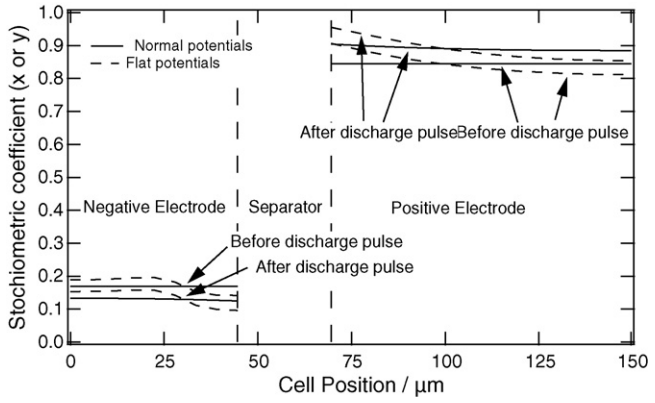

Fig. 20. Internal cell profiles of the stoichiometric coefficient x in Li_xC_6 or y in $Li_{y+0.16}Mn_{1.84}O_4$ immediately before and at the end of a 10*C* discharge pulse at a state-of-discharge of *ca.* 0.8. The results are for the $Li_xC_6/Li_{y+0.16}Mn_{1.84}O_4$ system with the HEV cell parameters.

Why do we not observe a similar effect in the $Li_xC_6/Li_{y+0.16}Mn_{1.84}O_4$ system with the HEV cell parameters? Fig. 20 shows the profiles inside the $Li_xC_6/Li_{y+0.16}Mn_{1.84}O_4$ system with HEV parameters at a similar SOD. For the system with the HEV cell parameters, the solid-phase concentration gradients across the electrodes are smaller both before and after the pulse;

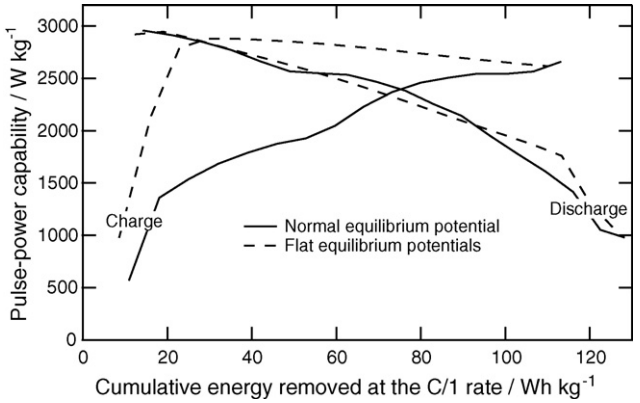

Fig. 18. Discharge and charge pulse-power capability of the $Li_xC_6/Li_{y+0.16}Mn_{1.84}O_4$ system with the PHEV cell parameters as a function of the cumulative energy removed at the *C*/1 rate. The charge power displayed here has been divided by 0.8 according to the USCAR manual.

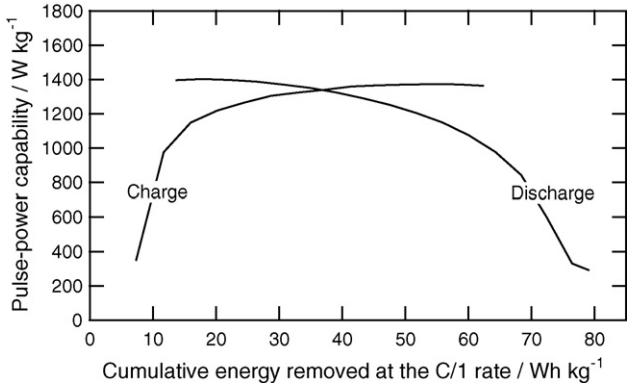

Fig. 21. Discharge and charge pulse-power capability of the $Li_{4+3x}Ti_5O_{12}/Li_yFePO_4$ system with the PHEV cell parameters as a function of the cumulative energy removed at the *C*/1 rate. The charge power displayed here has been divided by 0.8 according to the USCAR manual.

this is a result of a more uniform current distribution, typical of a system with thin electrodes [25]. To verify that this effect is not only a result of the "artificial" flat potentials that we use for the $Li_xC_6/Li_{y+0.16}Mn_{1.84}O_4$ system, we also show the pulse-power capability of the $Li_{4+3x}Ti_5O_{12}/Li_yFePO_4$ system with the PHEV cell parameters in Fig. 21. Here we see that the pulse-power capability on discharge is more sloped for discharge than for charge, again indicating the persistence of solid-phase concentration gradients within the electrodes for flat-potential systems.

5. Conclusions

A combined battery and vehicle model is required to capture the details of the complex relationships between battery chemistry (*e.g.*, magnitude of the cell potential, shape of the equilibrium potential curves, and internal resistance) and battery size, while a simplified model can be used to understand the basic relationships. For example, the ten-second pulse resistance defined by the HPPC method may not yield the correct values for the battery in its actual application. In general, defining the resistance is difficult because it depends on the magnitude of the applied current and the duration of the applied pulse (for the chemistries we examined, we found the resistance to vary by a factor of *ca.* 2 depending on the magnitude and duration of the pulse). While it is clear that a set of relatively flat pulse-power capability curves can improve capacity usage and decrease battery size, there are several scenarios in which switching to a set of flat equilibrium potentials may result in reductions in performance. For example, at some values of the SOD the potential of a sloped-potential system may be higher than a flat-potential system, resulting in a lower pulse-power capability for the flat-potential system. In addition, during a sequence of consecutive pulse discharges or consecutive pulse charges, the pulse-power capability of a flat-potential system may be worse because there is no driving force for the relaxation of solid-phase concentration gradients through the electrode depth. This is especially true for relatively thick electrodes, which typically have a more non-uniform current distribution. In practice the various aspects of cell chemistry are related, and the results from this work should be able to provide cell developers with an improved perspective on how they fit together to influence overall performance.

References

[1] P. Albertus, J. Newman, J. Power Sources 183 (2008) 376–380.
[2] Available from: http://www.uscar.org/commands/files_download.php?files_id=26 (Accessed 1/18/08).
[3] Available from: http://www.uscar.org/commands/files_download.php?files_id=118 (Accessed 1/18/08).
[4] Available from: http://www.uscar.org/commands/files_download.php?files_id=58 (Accessed 1/18/08).
[5] Available from: http://www.a123systems.com/#/applications/phev/pchart3/ (Accessed 5/29/08).
[6] C. Fellner, High-power batteries for use in hybrid vehicles, Thesis in Department of Chemical Engineering, University of California Berkeley, Berkeley, CA, 1998.
[7] C. Fellner, J. Newman, Journal of Power Sources 85 (2) (2000) 229–236.
[8] T. Markel, A. Simpson, Advanced Automotive Battery Conference, Baltimore, MD, May 17–19, 2006.
[9] T. Markel, A. Simpson, SAE Future Transportation Technology and IEEE Vehicle Power and Propulsion Joint Conferences, Chicago, IL, September 7–9, 2005.
[10] M. Anderman, Journal of Power Sources 127 (1–2) (2004) 2–7.
[11] O. Bitsche, G. Gutmann, Journal of Power Sources 127 (1–2) (2004) 8–15.
[12] E. Karden, S. Ploumen, B. Fricke, T. Miller, K. Snyder, Journal of Power Sources 168 (1) (2007) 2–11.
[13] R.F. Nelson, Journal of Power Sources 91 (1) (2000) 2–26.
[14] K.J. Kelly, M. Mihalic, M. Zolot, 17th Annual Battery Conference on Applications and Advances, Long Beach, CA, January 14–18, 2002.
[15] Tien Duong, Advanced Automotive Batteries Conference, Long Beach, CA, May 17, 2007.
[16] J. Christensen, V. Srinivasan, J. Newman, Journal of the Electrochemical Society 153 (3) (2006) A560–A565.
[17] V. Srinivasan, Equilibrium potential curve for Li_yFePO_4, 11/20/2007, personal communication.
[18] S. Stewart, Determination of Transport Properties and Optimization of Lithium-Ion Batteries, Ph.D. thesis, University of California, Berkeley, 2007.
[19] Available from: http://www.cchem.berkeley.edu/jsngrp/ (Accessed 1/28/2008).
[20] M. Doyle, T.F. Fuller, J. Newman, Journal of the Electrochemical Society 140 (6) (1993) 1525–1533.
[21] T.F. Fuller, M. Doyle, J. Newman, Journal of the Electrochemical Society 141 (1) (1994) 1–10.
[22] T.F. Fuller, M. Doyle, J. Newman, Journal of the Electrochemical Society 141 (4) (1994) 982–990.
[23] Available from: http://www.nrel.gov/vehiclesandfuels/energystorage/pdfs/aabc_presentation.pdf (Accessed 1/18/08).
[24] A. Pesaran, M. Keyser, Annual Battery Conference, Long Beach, CA, January 9–12, 2001.
[25] J. Newman, K.E. Thomas-Alyea, Electrochemical Systems, third ed., Wiley-Interscience, 2004.